Registration of Head Volume Images Using Implantable Fiducial Markers

Calvin R. Maurer, Jr., *Member, IEEE*, J. Michael Fitzpatrick,* *Member, IEEE*, Matthew Y. Wang, *Student Member, IEEE*, Robert L. Galloway, Jr., *Member, IEEE*, Robert J. Maciunas, and George S. Allen

***Abstract*—In this paper, we describe an extrinsic-point-based, interactive image-guided neurosurgical system designed at Vanderbilt University, Nashville, TN, as part of a collaborative effort among the Departments of Neurological Surgery, Computer Science, and Biomedical Engineering. Multimodal image-to-image (II) and image-to-physical (IP) registration is accomplished using implantable markers. Physical space tracking is accomplished with optical triangulation. We investigate the theoretical accuracy of point-based registration using numerical simulations, the experimental accuracy of our system using data obtained with a phantom, and the clinical accuracy of our system using data acquired in a prospective clinical trial by six neurosurgeons at four medical centers from 158 patients undergoing craniotomies to resect cerebral lesions. We can determine the position of our markers with an error of approximately 0.4 mm in X-ray computed tomography (CT) and magnetic resonance (MR) images and 0.3 mm in physical space. The theoretical registration error using four such markers distributed around the head in a configuration that is clinically practical is approximately 0.5–0.6 mm. The mean CT-physical registration error for the phantom experiments is 0.5 mm and for the clinical data obtained with rigid head fixation during scanning is 0.7 mm. The mean CT-MR registration error for the clinical data obtained without rigid head fixation during scanning is 1.4 mm, which is the highest mean error that we observed. These theoretical and experimental findings indicate that this system is an accurate navigational aid that can provide real-time feedback to the surgeon about anatomical structures encountered in the surgical field.**

***Index Terms*— Fiducial markers, image-guided surgery, image registration, point-based registration, registration accuracy, stereotactic therapy.**

I. Introduction

REGISTRATION is the determination of a one-to-one mapping or transformation between the coordinates in one space and those in another, such that points in the two spaces that correspond to the same anatomical point are mapped to each other. Registration of multimodal images makes it possible to combine different types of structural information [X-ray computed tomography (CT) and magnetic resonance (MR) images] and functional information [positron emission tomography (PET) and single photon emission tomography (SPECT) images] for diagnosis and surgical planning. Registration of images acquired with the same modality at different times allows quantitative comparison of serial data for longitudinal monitoring of disease progression/regression and postoperative follow up. Registration of preoperative images with the physical space occupied by the patient during surgery is a fundamental step in interactive, image-guided surgery techniques. Surgical navigation systems use the image-to-physical (IP) transformation to track in real time the changing position of a surgical probe on a display of the preoperative images. Stereotactic procedures use the transformation to direct a needle (stereotactic biopsy) or energy (stereotactic radiosurgery) to a surgical target (e.g., tumor) located in the images.

In this paper, we describe an extrinsic-point-based, interactive image-guided neurosurgical system designed at Vanderbilt University as part of a collaborative effort among the Departments of Neurological Surgery, Computer Science, and Biomedical Engineering [11], [14], [15], [31], [33], [34], [37]–[39], [57], [58]. Industrial development and manufacturing of this system has been carried out in conjunction with Johnson & Johnson Professional, Inc. (Randolph, MA). The trademark for the commercial system is ACUSTAR I Advanced Neurosurgical Navigation System. Multimodal image-to-image (II) and IP registration is accomplished using implantable markers. Physical space tracking is accomplished with optical triangulation. We investigate the theoretical accuracy of point-based registration using numerical simulations, the experimental accuracy of our system using data obtained with a phantom, and the clinical accuracy of our system using data from a prospective neurosurgical clinical trial [32].

Manuscript received October 18, 1996; revised March 18, 1997. Preliminary versions of this work were presented at the conferences Computer Assisted Radiology 1995 (Berlin, Germany, June 21–24, 1995) and Medical Imaging 1997 (Newport Beach, CA, February 22–28, 1997). The Associate Editor responsible for coordinating the review of this paper and recommending its publication was M. W. Vannier. *Asterisk indicates corresponding author.*

C. R. Maurer, Jr. and M. Y. Wang are with the Departments of Computer Science and Neurological Surgery, Vanderbilt University, Nashville, TN 37235 USA.

*J. M. Fitzpatrick is with the Departments of Computer Science, Neurological Surgery, and Radiology, Vanderbilt University, Nashville, TN 37235 USA (e-mail: jmf@vuse.vanderbilt.edu).

R. L. Galloway, Jr. and R. J. Maciunas are with the Departments of Biomedical Engineering and Neurological Surgery, Vanderbilt University, Nashville, TN 37235 USA.

G. S. Allen is with the Department of Neurological Surgery, Vanderbilt University, Nashville, TN 37232 USA.

Publisher Item Identifier S 0278-0062(97)05635-8.

II. Methods

A. Image Markers and Localization

The image markers are constructed from hollow plastic cylinders with an inside diameter $d = 7$ mm and an inside height $h = 5$ mm (see Figs. 1 and 2). The cylinders are filled with an aqueous solution of 165-mg/ml iothalamate

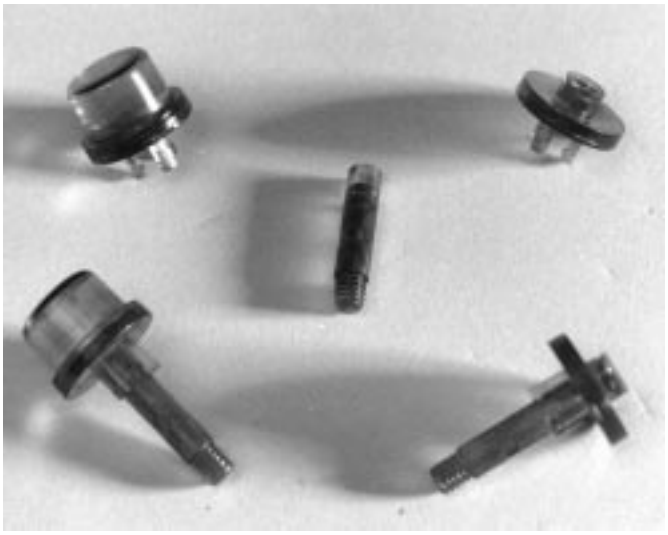

Fig. 1. Photograph of markers. The image markers (left) are constructed from hollow plastic cylinders with an inside diameter $d = 7$ mm and an inside height $h = 5$ mm. The cylinders are filled with an aqueous solution of 165 mg/ml iothalamate meglumine and 0.5-mM gadopentetate dimeglumine and sealed. The localization caps or physical space markers (right) are manufactured with a hemispherical divot whose position corresponds to the centroid of the image markers. The threaded ends of plastic marker bases or posts (middle) are screwed into the outer table of the skull of the patient. The base is 13 mm in length and 3 mm in diameter; the threaded end is 3 mm in length. The image markers are attached to the bases (bottom left) during image acquisition. The localization caps are attached to the bases (bottom right) intraoperatively.

meglumine[1] and 0.5-mM gadopentetate dimeglumine[2] and are sealed. The marker is bright in X-ray CT images because iodine attenuates X rays. The marker is bright in MR images because gadolinium reduces the T1 relaxation parameter of the hydrogen protons in the water. Fig. 3 shows the typical appearance of the markers in CT and MR images.

Markers are implanted after obtaining informed consent in accordance with Institutional Review Board approved clinical protocol guidelines. Implantation sites are selected on an individual basis, depending on clinical circumstances. Approximately 1 ml of local anesthetic is instilled subcutaneously at each site to minimize discomfort during application. After making a 3.5-mm skin incision, a sterile guide is advanced to the outer table of the skull and a premeasured drill is inserted to produce a 4-mm-deep anchoring hole. An applicator, preloaded with a marker base, is advanced down the guide cannula and the base is screwed into the bone of the skull. The plastic marker base is 13 mm in length and 3 mm in diameter; the threaded end is 3 mm in length (see Fig. 1). Marker bases may remain in place for weeks at a time. The image markers are attached to the bases during image acquisition. Plastic caps are used to cover and protect the markers. Patients can undergo surgery at any time after image acquisition. There is a risk of superficial infection at the implantation sites. Strict aseptic technique is utilized throughout the course of all implantations and prophylactic antibiotics are used (they are already routinely administered preoperatively for all neurosurgical procedures). No such infections have been observed in clinical results to date.

[1] Conray (Mallinckrodt Medical, Inc., St. Louis, MO).

[2] Magnevist (Berlex Laboratories, Wayne, NJ).

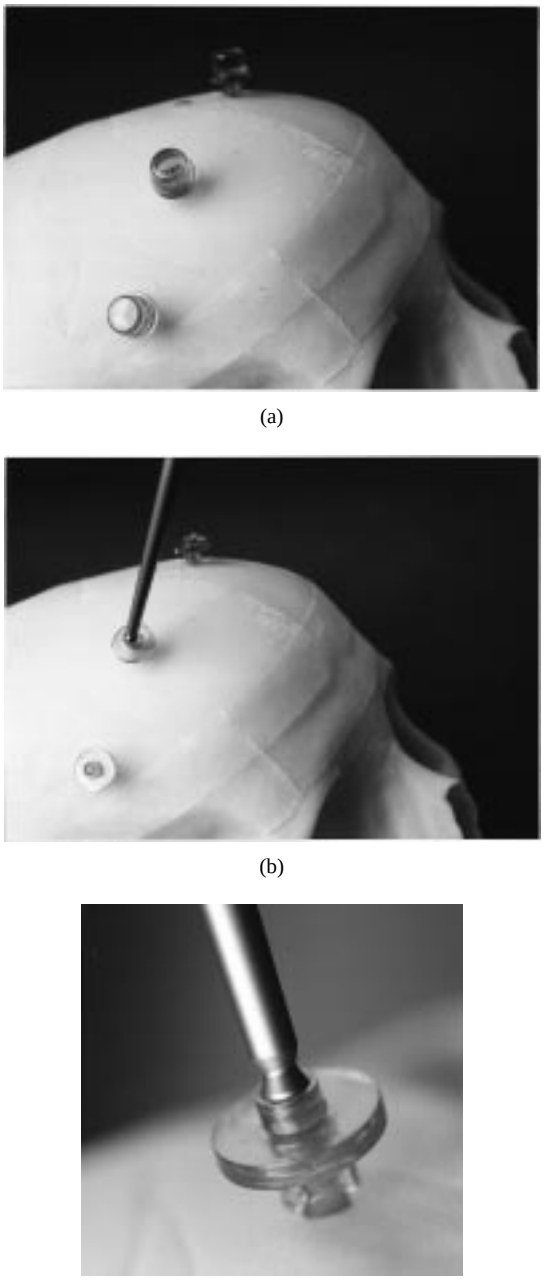

(a)

(b)

(c)

Fig. 2. Markers on skull phantom. (a) The image markers are attached to the bases during image acquisition. (b) The localization caps (physical space markers) are attached to the bases intraoperatively. (c) Physical space localization of the markers is performed by placing a localization probe with a 3-mm diameter spherical ball at its distal tip into the divot of each cap.

It is important to define carefully what point derived from a marker is going to be used for registration. We call the points used for registration *fiducial points* or *fiducials*. We define the fiducial point of an image marker as its centroid and call the determination of this position *fiducial localization*. We determine an intensity-weighted centroid for each marker using the fiducial localization method previously described in [58]. Briefly, the image is first searched for candidate markers. Then the neighborhood regions of the "seed" positions (voxels)

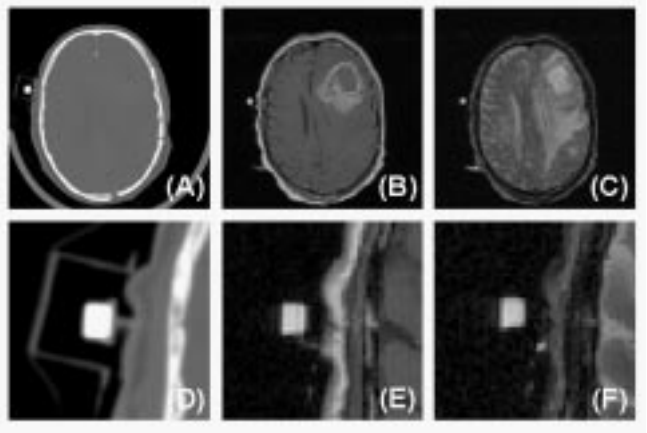

Fig. 3. Appearance of the image marker in CT and MR images. (a) is a transverse CT image slice of the head. (b) and (c) are transverse MR T1-weighted and T2-weighted spin-echo image slices, respectively. One marker appears in each of these slices. A plastic protective cap surrounding the marker is faintly visible in the CT image. (d)–(f) are enlargements of the markers in (a)–(c), respectively.

Fig. 4. Photograph of probe and probe attachment. The probe attachment is approximately 15-cm long and consists of a thermoplastic handle equipped with two pushbutton controls and an anodized aluminum housing containing an array of 19 IRED's. The identity of the tool and the configuration (relative position and orientation) of the rigid-body array of IRED's are stored in a chip at the end of the cable that connects the tool to the system. Marker localization is performed using a 10.5-cm-long probe constructed of anodized titanium alloy that tapers down to form a 3-mm-diameter spherical ball at its distal tip (shown). Surgical navigation is performed using a 13-cm-long probe with a 1.5-mm-diameter spherical tip (not shown).

of the candidate markers are divided into foreground (marker) and background voxels by thresholding, the set of foreground voxels that are three-dimensionally connected to the candidate voxel are identified by region growing, and an intensity-weighted centroid of the foreground component is calculated. The technique essentially finds the lowest threshold, such that the object formed from voxels whose intensities are higher than the threshold and that are three-dimensionally connected to the candidate marker voxel is neither too small nor too large to be a marker. If it is not possible to find such a threshold, the candidate marker is identified as a false marker and rejected. The marker positions produced by the algorithm are reviewed by the user in a graphical interface. False markers are discarded. In this case the user can interactively provide new seed positions to the second step of the algorithm.

We call the error of determining the positions of the markers *fiducial localization error* (FLE).[3] The FLE of image markers is different from the FLE of physical space markers (see Section II-B). We distinguish these FLE's by adding a subscript I (image markers) or P (physical space markers). FLE_I arises from a number of factors, including the digital nature of an image (spatial and intensity quantization), blurring and other distortions inherent in the imaging process, and noise. We have previously estimated FLE_I with numerical simulations [57], phantom experiments [39], and clinical trial data [38]. For the marker shape and size, voxel dimensions, and signal-to-noise ratio in our study, the FLE_I predicted by simulations is approximately 0.2 mm. The FLE_I estimated using phantom experiments and clinical trial data is approximately 0.4 mm for CT and MR images with slice thickness 3–4 mm. The FLE_I estimated with phantom data is a true measure of accuracy (as opposed to reproducibility) since these experiments registered localized image positions to physically known positions. The experimentally estimated FLE_I is higher than that predicted by numerical simulations, probably because of imperfect marker segmentation.

B. Physical Space Markers and Localization

Physical space tracking is accomplished with optical triangulation. We use an optical position sensor (OPS) that consists of three one-dimensional (1-D) charge-coupled device (CCD) arrays paired with three cylindrical lenses and mounted in a stabilized bar 1.1 m in length.[4] Each lens directs light from sequentially strobed infrared-emitting diodes (IRED's) onto a CCD. The three-dimensional (3-D) position of an IRED is determined from the positions of the light on the three CCD's. Each CCD provides a plane containing the IRED. With three CCD's the IRED position is essentially the intersection of these planes.

We are more interested in the position of a surgical tool than in the position of an individual IRED. Surgical probes are connected to a "probe attachment" consisting of a thermoplastic handle equipped with two push-button controls and an anodized aluminum housing containing an array of 19 IRED's (see Fig. 4). The identity of the tool and the configuration (relative position and orientation) of the rigid-body array of IRED's are stored in a chip at the end of the cable that connects the tool to the system. The system fits the detected IRED positions to the stored positions and, thus, provides the orientation of the probe and the position of the probe tip. The probe tip position is accepted only if at least four IRED's are detected, with at least one IRED from both the proximal and the distal probe attachment IRED clusters, and the residual error of the fit between the detected and stored IRED positions is less than 0.5 mm.

[3] When the markers are used as targets, we call this error *target localization error* (TLE).

[4] Optotrak 3020 (Northern Digital, Inc., Waterloo, Ont., Canada).

Fig. 5. Photograph of reference emitter. The reference emitter consists of five arms that form a 3-D cross containing an array of 20 IRED's, four on each of the five arms. The housing is constructed of anodized aluminum alloy. Each arm is approximately 6-cm long. The reference emitter is rigidly attached to the patient's head via a multijointed arm and a Mayfield skull clamp (the head fixation device).

Marker localization is performed using a 10.5-cm-long probe constructed of anodized titanium alloy that tapers down to form a 3-mm-diameter spherical ball at its distal tip (see Fig. 4). Surgical navigation is performed using a 13-cm-long probe with a 1.5-mm-diameter spherical tip. Each probe is calibrated by placing the probe tip in a fixed location and pivoting the probe about this fixed point. The position of the probe tip relative to the coordinate system of the probe attachment is determined by finding the most invariant point (in a least squares sense) in these pivot motions. The rms residual error is typically approximately 0.2 mm. The calibration is accepted only if the residual error is less than 0.5 mm, there is sufficient data (at least 160 points), and there is a reasonable range of pivot motion (at least 60° major axis, 45° minor axis).

A "reference emitter" (see Fig. 5) that consists of five arms forming a 3-D cross containing an array of 20 IRED's, four on each of the five arms, is rigidly attached to the patient's head via a multijointed arm and a Mayfield skull clamp (the head fixation device). The reference emitter position is accepted only if at least four IRED's from at least three arms are detected and the residual error of the fit is less than 0.175 mm. The reference emitter defines the intraoperative coordinate system. All surgical tool physical positions are reported in this reference coordinate system. This allows repositioning of the OPS when necessary, e.g., to maintain an optical line of sight.

The surgical tool position update rate depends on the number of "rigid bodies" (i.e., probe attachment, reference emitter) used and the total number of IRED's on these rigid bodies. With one surgical probe and a reference emitter, we obtain approximately 20 probe position (relative to reference coordinate system) updates per second.

Localization caps (physical space markers) are attached to the marker bases intraoperatively (see Figs. 1 and 2). These caps are manufactured with a hemispherical divot whose position corresponds to the centroid of the image markers. Physical space localization of the markers is performed by placing a localization probe with a 3-mm diameter spherical ball at its distal tip into the divot of each cap (see Fig. 2). We note that the ball-point tip pivots about the center of the ball rather than a point on the surface of the ball.

We estimated $\mathrm{FLE_P}$ to be approximately 0.3 mm by localizing physical space markers on a phantom milled by a machine with a stated accuracy of 0.001 in (0.025 mm). The accuracy of tip position using an identical OPS and similar probes has been reported by other investigators to be approximately 0.1 mm or better [44], [49], 0.1–0.2 mm [40], and 0.3 mm [30]. Our accuracy estimate is at the high end of these observations probably because $\mathrm{FLE_P}$ represents not only tip position accuracy but also manufacturing tolerances of the localization caps. Also, the excellent accuracy reported in [44] was obtained by keeping the probe in a fixed orientation with respect to the OPS. Our accuracy estimate was obtained by using the probe at many arbitrary orientations. We note that we accept only probe tip positions that are within a field-of-view (FOV) that is roughly $1.0 \times 1.2 \times 1.4$ m centered approximately 2.5 m from the OPS.

C. Point-Based Registration

Point-based registration involves the determination of the coordinates of corresponding points in different images and/or physical space and the estimation of a geometrical transformation using these corresponding points [33], [37]. We assume that registrations involving head images of the same patient are rigid-body transformations $\mathcal{T}(\mathbf{p}) = \mathbf{R}\mathbf{p} + \mathbf{t}$, where $\mathbf{R}$ is a 3×3 rotation matrix, $\mathbf{t}$ is a 3×1 translation vector, and $\mathbf{p}$ is a 3×1 position vector. Let $\mathcal{P} = \{\mathbf{p}_j\}$ for $j = 1, \cdots, N$ be a point set to be registered with another point set $\mathcal{Q} = \{\mathbf{q}_j\}$ for $j = 1, \cdots, N$, where each point $\mathbf{p}_j$ corresponds to the point $\mathbf{q}_j$ with the same index. We wish to find the rigid-body transformation $\mathcal{T}$ that minimizes the cost function

$$d(\mathcal{T}) = \sqrt{\frac{1}{N}\sum_{j=1}^{N} \|\mathbf{q}_j - \mathcal{T}(\mathbf{p}_j)\|^2}\,. \tag{1}$$

This problem was given the name "orthogonal procrustes" problem by Hurley and Cattell [24]; it is known as the "absolute orientation" problem in photogrammetry [16]. A unique solution exists if and only if the point sets $\mathcal{P}$ and

$\mathcal{Q}$ contain at least three noncollinear points. A closed-form solution was first discovered by Schönemann in 1966 [47]. Many other closed-form solutions have been independently discovered. We use the solution of Arun *et al.* [2]. The method decouples the calculations of the rotation and translation parameters. The rotation matrix is computed using the singular value decomposition (SVD) of the covariance matrix of the centroid-subtracted position vectors in the two spaces. The translation vector is calculated as the difference between the centroids of the two sets of fiducials.

We calculate a rigid-body transformation for each fiducial correspondence permutation. An exhaustive search takes less than 1 s on current workstations for $N \leq 10$. The transformation obtained by the fiducial correspondence that produces the smallest value of the cost function in (1) is presented to the user. It is possible that the fiducials will be approximately rotationally symmetric and, thus, that the correspondence producing the smallest value of the cost function is not the correct correspondence. Thus, the user must manually verify the presented transformation. If this transformation is not correct, the user can examine any of the four transformations obtained by the fiducial correspondences that produce the four smallest values of the cost function. We note that the minimum rotation angle between various permutations of approximately symmetric fiducials is $2\pi/N$ radians which is $\pi/2$ radians (90°) for $N = 4$ fiducials. Thus, the user will never need to distinguish between nearly identical transformations but rather merely verify that a presented transformation is not grossly wrong. We also provide the user the option of manually specifying the fiducial correspondence.

One measure of registration accuracy is the distance between corresponding fiducials after registration and transformation, i.e., the minimum value of the cost function in (1). We call this measure *fiducial registration error* (FRE). A more objective measure of registration accuracy is the distance between corresponding points other than those used to estimate the transformation parameters. Because such points might represent surgical targets, we call such points *targets* and the corresponding accuracy measure *target registration error* (TRE). When we use the term "registration error," without a modifier, we mean TRE.

D. Numerical Simulations

The head is modeled as a sphere of radius $R = 100$ mm. The numerical simulations are performed as follows.

1) Specify the fiducial points $\mathcal{P} = \{\mathbf{p}_j\}$ for $j = 1, \cdots, N_f$ in space S_1. We place the fiducials on the surface of the sphere.
2) Specify the target points $\mathcal{U} = \{\mathbf{u}_k\}$ for $k = 1, \cdots, N_t$ in space S_1. We place the targets within the sphere on a 3-D grid at 1-mm intervals in each direction. Alternatively, we place the targets randomly on the surface of the sphere.
3) Specify the fiducial localization errors FLE_1 and FLE_2 in spaces S_1 and S_2, respectively.
4) Specify the target localization errors TLE_1 and TLE_2 in spaces S_1 and S_2, respectively.
5) Repeat the following steps $M = 10\,000$ times[5]:
   a) Copy the fiducial positions $\mathcal{P}$ in space S_1 to $\mathcal{Q} = \{\mathbf{q}_j\}$ in space S_2.
   b) Copy the target positions $\mathcal{U}$ in space S_1 to $\mathcal{V} = \{\mathbf{v}_k\}$ in space S_2.
   c) Simulate the localized fiducial positions by randomly and independently perturbing $\mathcal{P}$ and $\mathcal{Q}$ using FLE_1 and FLE_2, respectively.
   d) Simulate the localized target positions by randomly and independently perturbing $\mathcal{U}$ and $\mathcal{V}$ using TLE_1 and TLE_2, respectively.
   e) Compute the rigid-body transformation $\mathcal{T}$ that registers the perturbed fiducial positions $\mathcal{P}$ with $\mathcal{Q}$.
   f) Compute FRE using (1).
   g) Compute TRE for each target as $||\mathbf{v}_k - \mathcal{T}(\mathbf{u}_k)||$.

The space S_1 represents an image coordinate space; S_2 can represent either an image or a physical coordinate space. If TLE is set to zero, then the resulting TRE represents the "true" registration error. If TLE is set to FLE, then the resulting TRE represents the registration error that would be "observed" when markers used to estimate the transformation are of the same type as (but distinct from) markers used to calculate registration accuracy. We distinguish these TRE's by adding a subscript T (true) or O (observed). If the targets are placed within the sphere, the resulting TRE represents the registration error averaged over the volume. If the targets are placed on the surface of the sphere, the resulting TRE represents the registration error averaged over the surface. We distinguish these TRE's by adding a subscript V (volume) or S (surface). Thus, TRE_{OS} is the registration error observed on the surface.

We use normal localization error component distributions and isotropic component variances (i.e., $\sigma_x = \sigma_y = \sigma_z = \text{FLE}/\sqrt{3}$). We note that we could apply an arbitrary transformation to the fiducials/targets $\mathcal{P}/\mathcal{U}$ or $\mathcal{Q}/\mathcal{V}$ between steps 5-b) and 5-c) to simulate different patient positioning or different scan orientation. There will be some difference in the results for anisotropic perturbations, since the anisotropy will be oriented differently in the two spaces. There will be no difference for isotropic perturbations, and little difference for anisotropic perturbations if the scans are all acquired in approximately the same orientation (e.g., transverse).

E. Phantom Experiments

We evaluate the experimental accuracy of our system using a multitiered plastic phantom that is hollowed out creating various internal levels (see Figs. 6 and 7). The phantom is designed to roughly approximate the size and shape of a human head. A total of 40 marker bases are mounted on the various internal and external levels, of which 20 were used in the experiments in this study. Twelve of these markers are positioned to represent external fiducial markers and are used for registration. The remaining eight markers are positioned to represent internal anatomy and are used as targets for assessment of registration accuracy. Fig. 6 shows a drawing

[5]We perform 10 000 iterations per simulation because we found that with this number we obtain mean TRE values that differ by less than 1% when a simulation is repeated with a different random seed.

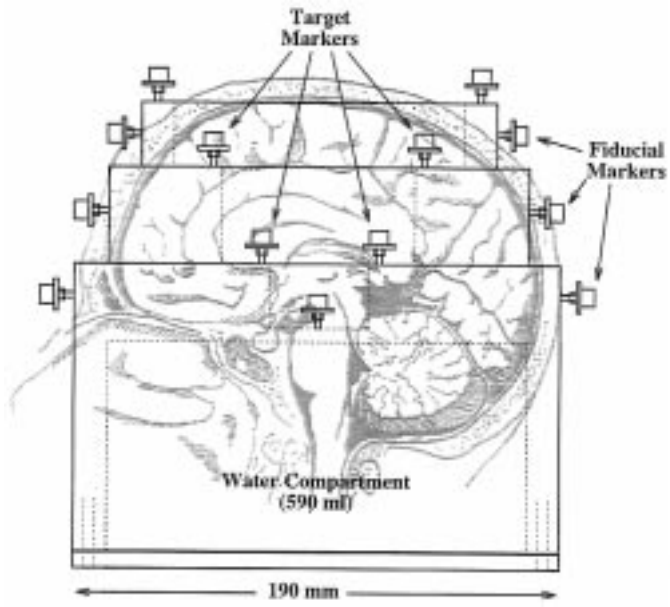

Fig. 6. Schematic drawing of side view of phantom. The multitiered plastic phantom is hollowed out creating various internal levels. It is designed to roughly approximate the size and shape of a human head. The placement of markers on the phantom simulates representative positions for external fiducial markers and internal anatomical targets. A drawing of a head is superimposed to illustrate how the configuration of markers corresponds to anatomy.

of a head superimposed on a side view of the phantom and illustrates how the configuration of markers corresponds to anatomy. The 12 fiducial markers are divided into three sets such that each set contains four markers evenly distributed around the phantom. Each fiducial set is used to compute a rigid-body transformation. Each target is used to compute one TRE value using one of the transformations determined with the three fiducial sets.

The phantom was sent to four medical centers.[6] At each site, one CT and one MR T1-weighted (T1) spin-echo image of the phantom were acquired.[7] Image markers are attached to the marker bases during image acquisition. Also at each site, physical space measurements were made as follows. The phantom is rigidly fixed in a Mayfield skull clamp using actual skull pins in the same manner that a head would be secured in the operating room (see Fig. 7). There are three divots on the outside surface of the phantom that mate with the skull pins. Physical space markers (localization caps) are attached to the marker bases. The reference emitter is attached to the skull clamp via a multijointed arm. The OPS is positioned approximately 2.5 m from the phantom. Since we accept only probe tip positions that are within a limited FOV, the location of the reference emitter is overlayed on top and side projections of this FOV and displayed on the computer screen during OPS positioning. The localization probe is calibrated. Finally, the physical space markers are localized by placing the probe into the divot of each cap. At two sites, physical space localization was repeated once per hour for ten hours.

[6] Site 1: Vanderbilt University, Nashville, TN. Site 2: Scripps Clinic, La Jolla, CA. Site 3: Western Pennsylvania Hospital, Pittsburgh, PA. Site 4: University of Washington, Seattle, WA.

[7] Except that no MR images were acquired at Site 3.

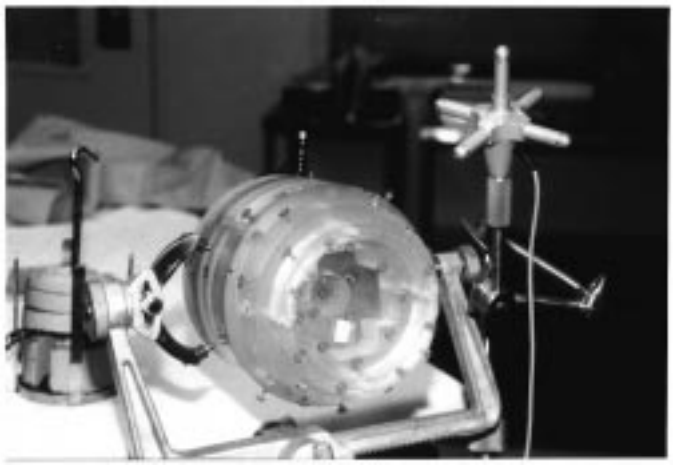

Fig. 7. Photograph of phantom during physical space localization experiment. The phantom is rigidly fixed in a Mayfield skull clamp using actual skull pins. Physical space markers (localization caps) are attached to the marker bases. The reference emitter is attached to the skull clamp via a multijointed arm. The OPS is behind the camera.

TABLE I
NUMBER OF PATIENTS FROM EACH SITE IN EACH PHASE

	Site 1	Site 2	Site 3	Site 4	Total
Phase I	15	7	10	10	42
Phase II	55	12	13	36	116
Total	70	19	23	46	158

During these experiments, the OPS was moved one or two feet between hours three and four, and again between hours six and seven to simulate the repositioning that is occasionally necessary intraoperatively, e.g., to maintain an optical line of sight.

F. Clinical Trial Data

We evaluate the clinical accuracy of our system using data acquired in a prospective clinical trial between February 1994 and May 1996 by six neurosurgeons at four medical centers[6] from 158 patients undergoing craniotomies to resect cerebral lesions. Most of the craniotomies were performed for gliomas (97 of 158 cases). The system was also used in cases of other types of tumors, abscess, and primary epilepsy. Each patient had five markers implanted. Four of the markers are used as fiducials for registration; the fifth is used as a target for assessment of registration accuracy. The markers used as targets were specified by the surgeons preoperatively. The markers were generally widely distributed about the head, with two of the fiducial markers inferior and two superior to the region of surgical interest. The exact locations of the markers were chosen according to individual clinical circumstances. The clinical trial consisted of two phases. Patients in Phase I had a stereotactic head frame applied. The frame was attached to the scanner table during image acquisition. The frame served as a redundant reference system that was, in fact, never needed. It also served as a head fixation device. Patients in Phase II

TABLE II
DESCRIPTION OF THE PHANTOM AND CLINICAL CT AND MR IMAGE VOLUMES

Study	Modality	Resolution		Voxel Size (mm)		MR Imaging Parameters	
		x, y	z	x, y	z	TE (ms)	TR (ms)
Phantom Experiments	CT	512	35–40	0.65	3.0	N/A	N/A
	MR T1	256	26	1.25	4.0	15	650
Clinical Trial	CT	512	28–55	0.42–0.65	3.0–5.0	N/A	N/A
	MR T1	256	26–52	0.80–1.25	3.0–5.0	10 15	600–800
	MR PD	256	26	0.80–1.25	3.0–5.0	20	3000
	MR T2	256	26	0.80–1.25	3.0–5.0	80–108	3000–4000

All image volumes are stacks of transverse image slices with no interslice gap or slice overlap. The x/y resolution is the number of pixels in each direction in each image slice. The z resolution is the number of slices in the image volume. The x/y voxel size is the pixel size. The z voxel size is the slice thickness.

did not have a frame applied. The number of patients from each site in each phase is listed in Table I.

One CT and one or more MR T1, PD-weighted (PD), and/or T2-weighted (T2) spin-echo MR images were acquired preoperatively for most patients. [7] Imaging studies were performed the day before or on the morning of the surgical procedure after implantation of the marker bases. Image markers are attached to the bases just prior to image acquisition. Intraoperatively, the head is fixed, localization caps are attached to the marker bases, the reference emitter is attached via a multijointed arm, the OPS is positioned, the localization probe is calibrated, and the physical space markers are localized. For 24 patients in Phase II, localization of the target marker was repeated several times during surgery.

G. Image Acquisition

The CT images were acquired using a Siemens Somatom Plus (Site 1), GE High Speed (Sites 2 and 4), or GE High Speed RP (Site 3) scanner. The MR images were acquired using either a Siemens SP 1.5 T (Site 1) or GE Signa 1.5 T (Sites 2 and 4) scanner.[7] The slice thickness of most of the CT and MR images is 3.0 mm and 4.0 mm, respectively. All image volumes are stacks of transverse image slices with no interslice gap or slice overlap. All phantom MR images were obtained using the body coil. All clinical MR images were obtained using a head coil except for the MR images in Phase I at Site 1. The latter were obtained using the body coil because the stereotactic frame will not fit within the head coil. A description (image resolution, pixel size, slice thickness, and MR echo time TE and repetition time TR) of the phantom and clinical images is listed in Table II. Images were transferred to a surgical planning workstation via network. After fiducial localization and treatment planning, the original images plus any optionally created reformatted and rendered images were transferred to an operating room workstation via optical disk.

H. Geometrical Distortion Correction

For the phantom MR images at Site 1 and the clinical MR images in Phase I at Site 1, additional MR images were acquired with the identical imaging parameters, except that the readout and preparation gradients were reversed. We correct these MR images for geometrical distortion caused by static field inhomogeneity by using the technique described in [6], [35]. A new image, without geometrical distortion, is generated from a pair of distorted images acquired with reversed readout gradients. The rectified images were not used in the clinical trial for preoperative planning or intraoperative navigation.

III. RESULTS

A. Numerical Simulations

The numerical simulations reveal that for a given fiducial configuration, TRE is proportional to $\mathrm{FLE}_{\mathrm{eff}}$, where the quantity $\mathrm{FLE}_{\mathrm{eff}}$ is defined as

$$\mathrm{FLE}_{\mathrm{eff}} = \sqrt{\frac{\mathrm{FLE}_1{}^2 + \mathrm{FLE}_2{}^2}{2}} \tag{2}$$

and where FLE_1 and FLE_2 are the FLE's in spaces S_1 and S_2, respectively. This result is illustrated in Fig. 8 for several fiducial configurations. The quantity $\mathrm{FLE}_{\mathrm{eff}}$ is an "effective" FLE. That is, regardless of the ratio $\mathrm{FLE}_1/\mathrm{FLE}_2$, the registration is statistically equivalent to a registration produced with $\mathrm{FLE}_1 = \mathrm{FLE}_2 = \mathrm{FLE}_{\mathrm{eff}}$. This finding allows us to more generally summarize numerical simulation results by using the dimensionless ratio $\mathrm{TRE}/\mathrm{FLE}_{\mathrm{eff}}$. The numerical simulations further reveal that $\mathrm{TRE}/\mathrm{FLE}_{\mathrm{eff}}$ is roughly inversely proportional to the square root of the number of fiducials. This result is demonstrated in Fig. 9.

We investigated the effect of fiducial location on TRE for four fiducials. We examined a tetrahedral arrangement plus the four fiducial configurations illustrated in Fig. 10. In Cases A–C, the fiducials are placed in the transverse plane passing through the center of the head. In Case D, the fiducials are placed in a square in a sagittal plane not passing through the center of the head. Case A is a "2-2" configuration, i.e., two fiducials are positioned on each side of the head. Case B is a 3-1 configuration. Cases C and D are 4-0 configurations. For the tetrahedral arrangement, and also for the case of four fiducials distributed evenly around the circumference

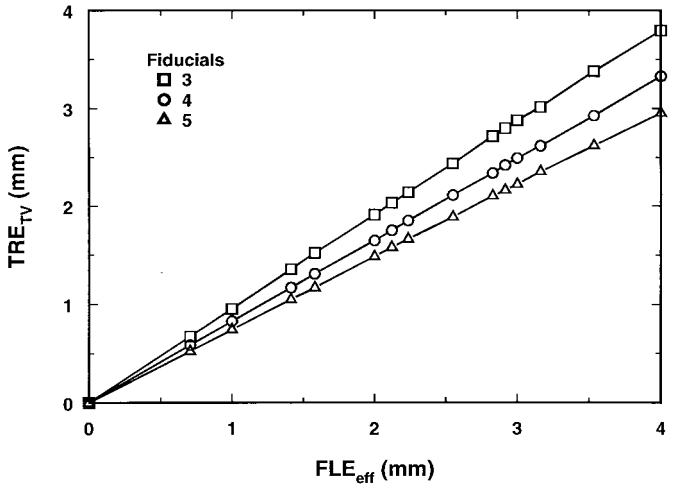

Fig. 8. Relationship between TRE and FLE. This figure illustrates that TRE is proportional to $\mathrm{FLE}_{\mathrm{eff}}$. This is shown for the cases of three, four, and five fiducials distributed evenly around the circumference of a sphere of radius 100 mm. Each symbol represents the mean theoretical $\mathrm{TRE}_{\mathrm{TV}}$ predicted by numerical simulation using a pair of FLE_1 and FLE_2 values formed from the set of localization errors {0, 1, 2, 3, and 4 mm}. All 15 possible pairs were used.

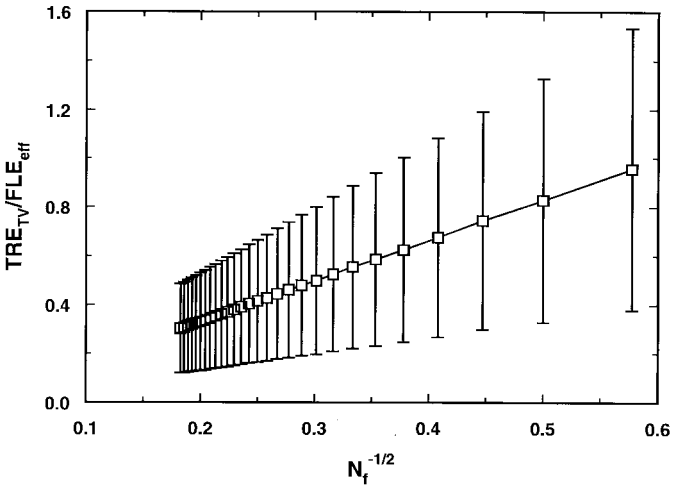

Fig. 9. Relationship between TRE and the number of fiducials. This figure illustrates that TRE is inversely proportional to the square root of the number of fiducials N_f. The symbols and error bars represent theoretical $\mathrm{TRE}_{\mathrm{TV}}/\mathrm{FLE}_{\mathrm{eff}}$ values (mean $\pm$ SD) predicted by numerical simulation. The number of fiducials varies from three (far right) to 30 (far left). The fiducials were distributed evenly around the circumference of a sphere of radius 100 mm.

of the head (which is Case A with $d = 2\pi R/4 = 157$ mm), $\mathrm{TRE}_{\mathrm{TV}}/\mathrm{FLE}_{\mathrm{eff}} = 0.82 \pm 0.37$ (mean $\pm$ SD).[8] These fiducial configurations appear to be optimal since we have not found any arrangement that provides more accurate registration. Fig. 11 quantifies how registration accuracy degrades as the fiducials are distributed less evenly around the head. For Case A, registration is "very accurate" (mean $\mathrm{TRE}_{\mathrm{TV}}/\mathrm{FLE}_{\mathrm{eff}} < 1.2$) for $d > 50$ mm. We examined more realistic variations of Case A, i.e., 2-2 configurations where the distances between fiducials on the two sides are different

[8] Any difference between the mean $\mathrm{TRE}_{\mathrm{TV}}/\mathrm{FLE}_{\mathrm{eff}}$ of these two configurations is < 0.01.

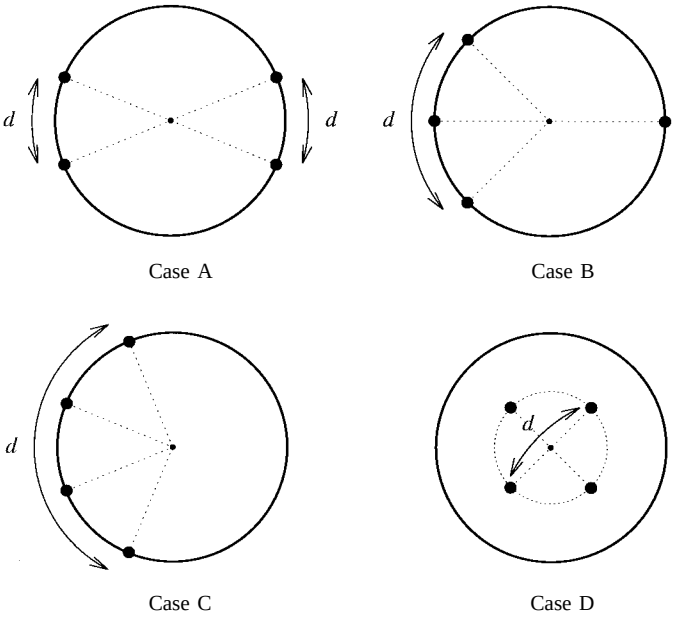

Fig. 10. Fiducial configurations examined. This figure illustrates four ways that four fiducials were positioned on the surface of the head, which is modeled as a sphere of radius 100 mm. In Cases A through C, the fiducials were placed in the transverse plane passing through the center of the head. In Case D, the fiducials were placed in a square in a sagittal plane not passing through the center of the head. The figure for this case is a lateral projection. The dotted circle represents the intersection of the sagittal plane and the head surface. In all cases, d is the maximum distance between fiducials on one side of the head. We define d not as Euclidean distance but rather as distance along the surface.

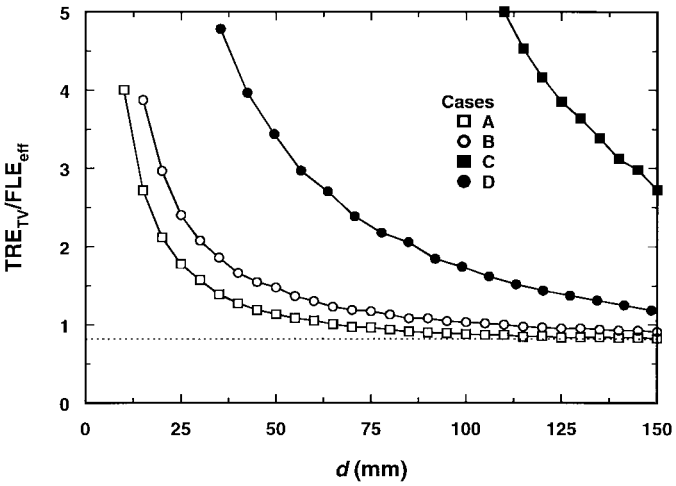

Fig. 11. Effect of distance between fiducials on TRE. Each symbol represents the mean theoretical $\mathrm{TRE}_{\mathrm{TV}}/\mathrm{FLE}_{\mathrm{eff}}$ predicted by numerical simulation for one of the four fiducial configurations shown in Fig. 10. The x-axis is the distance d in that figure. The dotted line is the mean $\mathrm{TRE}_{\mathrm{TV}}/\mathrm{FLE}_{\mathrm{eff}}$ when the four fiducials are distributed evenly around the circumference of the head (e.g., Case A, $d = 2\pi R/4 = 157$ mm).

and where the fiducials are not coplanar. We found that the accuracy of any 2-2 fiducial configuration is determined primarily by the larger of the distances between fiducials on the two sides. The accuracy of any 2-2 configuration is, thus, approximately described by the curve for Case A in Fig. 11 where d is taken to be this larger distance. For Case B, registration is very accurate (mean $\mathrm{TRE}_{\mathrm{TV}}/\mathrm{FLE}_{\mathrm{eff}} < 1.2$)

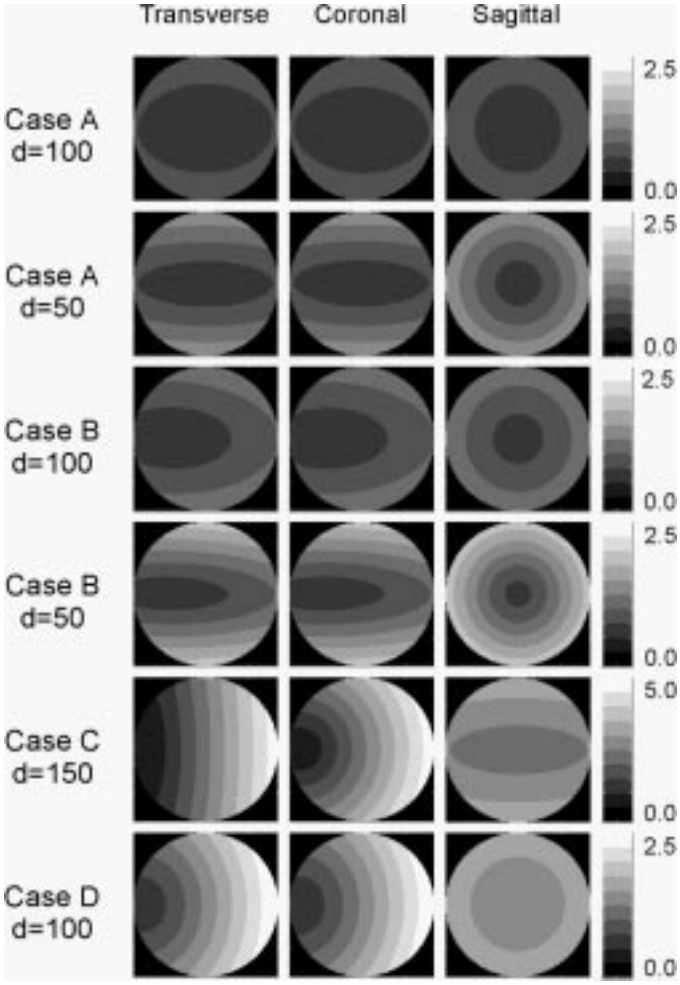

Fig. 12. Triplanar views of the spatial distribution of TRE/FLE_{eff} for the four fiducial configurations shown in Fig. 10 with various values of d. Values of d are in units of mm. Inside the head, mean values of TRE/FLE_{eff} are quantized and displayed as a gray value. Regions outside the head are set to black. Note that the scale for Case C (0–5 mm) is different from the scale for all other cases (0-2.5 mm).

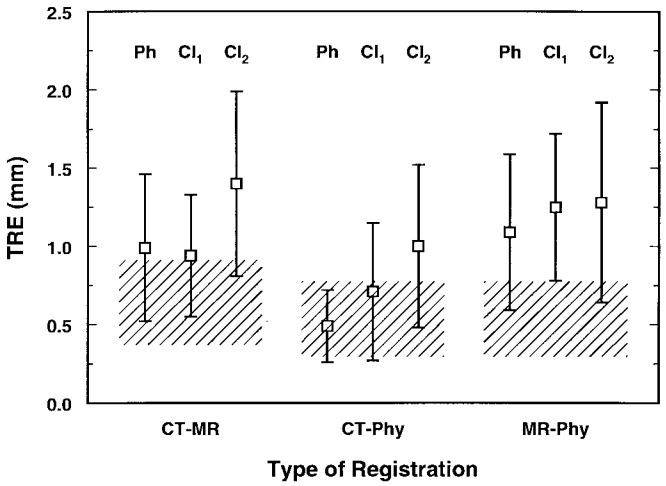

Fig. 13. Summary of theoretical, phantom, and clinical registration accuracy. The symbols and error bars represent the experimental and clinical TRE values (mean $\pm$ SD) calculated by pooling the phantom (Ph) and clinical trial Phase I (Cl_1) and Phase II (Cl_2) data from all sites. The hatched areas represent theoretical TRE_{OS} values (mean $\pm$ SD) predicted by numerical simulation. See Table III for additional information.

for $d > 75$ mm. We also examined variations of Case B. We found that the accuracy of any 3-1 fiducial configuration is determined primarily by the maximum distance between any two of the three fiducials that are on one side of the head. Unfortunately, no such simple generalization appears to hold for 4-0 configurations. Cases C and D represent opposite extremes of such fiducial arrangements. In Case C, the fiducials are arranged in an arc. The accuracy of registration for this configuration is "poor" (mean $\text{TRE}_{\text{TV}}/\text{FLE}_{\text{eff}} > 2.5$ for $d = 150$ mm) because the fiducials are quasicollinear and, thus, small errors in estimating their positions can cause large rotational errors about their principal axis. This effect is clearly demonstrated in the plots of spatial distribution of TRE shown in Fig. 12. The registration accuracy of Case D is better than that of Case C but considerably worse than that of Cases A and B. We found the accuracies of all 4-0 fiducial configurations we examined to be intermediate between the accuracies of Cases C and D. However, we note that these observations refer to accuracy averaged over the entire volume inside the head. Examination of Fig. 12 reveals that the accuracy of a 4-0 configuration near the surface on the side of the head where the markers are located can be comparable to the volume-averaged accuracy of a 2-2 or 3-1 configuration.

In summary, mean TRE_{TV} is approximately 0.8 FLE_{eff} for optimal configurations of four fiducials (i.e., a tetrahedral arrangement or a uniform distribution around the circumference) and less than 1.2 FLE_{eff} for many clinically practical configurations (i.e., a 2-2 configuration with $d > 50$ mm or a 3-1 configuration with $d > 75$ mm). For our system, FLE_{eff} is approximately 0.4 mm for II registration and 0.35 mm for IP registration (FLE_{I} and FLE_{P} are approximately 0.4 and 0.3 mm, respectively). Thus, numerical simulations predict that the mean TRE_{TV} of our system is approximately 0.3 mm for optimal configurations of four fiducials for both II and IP registration, and less than 0.5 mm for practical configurations.

The experimental and clinical TRE's were assessed using "internal" and "external" markers, respectively. Thus, these measurements are analogous to theoretical TRE_{OV} and TRE_{OS}, respectively. Theoretical values of TRE_{TV}, TRE_{TS}, TRE_{OV}, and TRE_{OS} for our system using an optimal configuration of four fiducials are listed in Table III. TRE_{OS} is only slightly larger than TRE_{OV} but is considerably larger than TRE_{TV}. Thus, the "observed" experimental and clinical TRE's are numerically similar quantities and provide a conservative estimate of the "true" TRE.

B. Phantom Experiments and Clinical Trial Data

The system was used in 158 operations performed by six neurosurgeons at four medical centers (see Table I). CT images were used in 120 operations and MR in 127 (CT only in 31, MR only in 38, CT and MR in 89). All presurgical planning and intraoperative navigation were performed using registration transformations computed using four markers as fiducials. Postoperative assessment of registration accuracy was performed by using the fifth marker as a target. We calculated CT-MR, CT-physical, and MR-physical TRE whenever

TABLE III
SUMMARY OF THEORETICAL, PHANTOM, AND CLINICAL REGISTRATION ACCURACY

Study	CT-MR			CT-Physical			MR-Physical		
	mean ± SD	95%	n	mean ± SD	95%	n	mean ± SD	95%	n
Simulations – TRE_{TV}	0.33 ± 0.15	0.61	10,000	0.29 ± 0.13	0.54	10,000	0.29 ± 0.13	0.54	10,000
Simulations – TRE_{TS}	0.38 ± 0.17	0.68	10,000	0.33 ± 0.15	0.60	10,000	0.33 ± 0.15	0.60	10,000
Simulations – TRE_{OV}	0.62 ± 0.26	1.09	10,000	0.55 ± 0.23	0.96	10,000	0.55 ± 0.23	0.96	10,000
Simulations – TRE_{OS}	0.64 ± 0.27	1.13	10,000	0.57 ± 0.24	1.00	10,000	0.57 ± 0.24	1.00	10,000
Phantom experiments	0.99 ± 0.47	1.86	9	0.49 ± 0.23	0.93	12	1.09 ± 0.50	2.02	9
Clinical trial – Phase I	0.94 ± 0.39	1.68	64	0.71 ± 0.44	1.61	39	1.25 ± 0.47	2.00	66
Clinical trial – Phase II	1.40 ± 0.59	2.44	135	1.00 ± 0.52	1.78	63	1.28 ± 0.64	2.51	190

This table lists theoretical TRE values predicted by numerical simulation and experimental and clinical TRE values calculated by pooling the phantom and clinical trial data from all sites. The simulations were performed for the case of four fiducials distributed evenly (i.e., ideally) around the circumference of the head with $FLE_I = 0.4$ mm and $FLE_P = 0.3$ mm. The 95% TRE values were determined by sorting the TRE values in ascending order and taking the $\lceil 0.95n \rceil th$ element in the sorted list. When $n < 20$, the 95% value is the same as the maximum value. The n values are the number of registrations performed. All TRE values are in units of mm.

TABLE IV
EFFECT OF GEOMETRICAL DISTORTION CORRECTION IN MR IMAGES ON PHANTOM AND CLINICAL REGISTRATION ACCURACY

Study	Dist. Corr.	CT-MR			CT-Physical			MR-Physical		
		mean ± SD	95%	n	mean ± SD	95%	n	mean ± SD	95%	n
Phantom experiments	No	0.92 ± 0.44	1.74	3	0.68 ± 0.31	1.28	3	1.07 ± 0.52	2.02	3
Clinical trial – Phase I	No	0.92 ± 0.39	1.72	39	0.74 ± 0.28	1.19	15	1.18 ± 0.45	1.98	39
Phantom experiments	Yes	0.63 ± 0.23	1.07	3	N/A			0.76 ± 0.32	1.37	3
Clinical trial – Phase I	Yes	0.71 ± 0.31	1.30	36	N/A			0.88 ± 0.41	1.62	36

This table lists experimental and clinical TRE values calculated using the phantom and clinical trial Phase I data from Site 1 before and after correction of geometrical distortion in MR images. The reversed readout gradient images necessary for distortion correction were not acquired at any other site nor in Phase II at Site 1. The CT-physical TRE values are listed to allow a comparison of results in this table, which were calculated using data from Site 1, with results in Table III, which were calculated using data pooled from all four clinical sites. The 95% TRE values were determined by sorting the TRE values in ascending order and taking the $\lceil 0.95n \rceil$th element in the sorted list. When $n < 20$, the 95% value is the same as the maximum value. The n values are the number of registrations performed. The number of registrations for the clinical data after distortion correction is slightly smaller than the number before correction because reversed readout gradient images were not acquired in three cases. All TRE values are in units of mm.

possible (e.g., if only CT images were acquired, then only CT-physical TRE could be calculated). We calculated CT-MR and MR-physical TRE for T1, PD, and T2 whenever possible. If two images of the same type were acquired (e.g., T1 before and after injection of gadopentetate dimeglumine), we used only the first one. In three cases, one of the markers was not present in the image FOV. In four cases, blood from the implantation skin incision accumulated in the plastic protective cover and prevented image localization of one of the markers. In one case, the marker base did not reach the bone. Thus, there was a technical problem that prevented the use of 8 of 784 total markers, i.e., approximately 1% of the markers. In all of these cases the four remaining markers were used for registration. In several other cases, only four markers were implanted, or only four markers were localized in physical space. Thus, we calculated TRE values using data acquired from 141 of the 158 operations in the clinical trial.

There is no significant difference in registration accuracy among the four sites for CT-MR, CT-physical, and MR-physical registrations for the phantom and clinical trial Phase I and Phase II data.[9] Similarly, there is no significant difference among T1, PD, and T2 for CT-MR and MR-physical.[9] Thus, the CT-MR, CT-physical, and MR-physical TRE values were pooled across the four sites and the three types of MR images. The pooled results are listed in Table III and plotted in Fig. 13. The registration accuracy in Phase I is not significantly different from that in the phantom experiments for CT-MR, CT-physical, and MR-physical registrations.[9] The accuracy in Phase II is not significantly different from that in the phantom experiments or Phase I for MR-physical.[9] However, the accuracy in Phase II is significantly worse than that in the phantom experiments and Phase I for CT-MR and CT-physical.[9] IP registration is significantly more accurate using CT images than MR in the phantom experiments and Phase I, but is not significantly different in Phase II.[10]

[9] Analysis of variance (ANOVA), $p = 0.05$. When ANOVA showed significant difference, individual comparisons were performed with Duncan's multiple range test. All statistical analysis was performed using SPSS for Windows Release 6.0 (SPSS, Inc., Chicago, IL).

[10] Two-tailed unpaired t-test, $p = 0.05$.

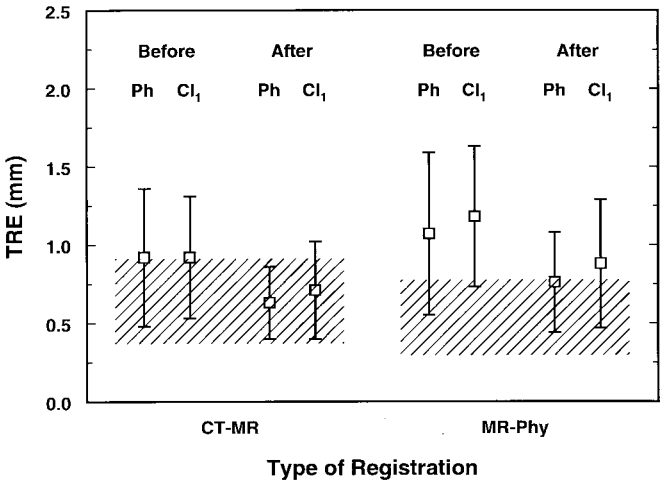

Fig. 14. Effect of geometrical distortion correction on phantom and clinical registration accuracy. The symbols and error bars represent the experimental and clinical TRE values (mean ± SD) calculated using the phantom (Ph) and clinical trial Phase I (Cl_1) data from Site 1 before and after correction of geometrical distortion in MR images. The hatched areas represent theoretical TRE_{OS} values (mean ± SD) predicted by numerical simulation. See Table IV for additional information.

We examined the effect of geometrical distortion correction on registration accuracy by calculating CT-MR and MR-physical TRE for the phantom and clinical trial Phase I data from Site 1 using uncorrected and corrected MR images. The results are listed in Table IV and plotted in Fig. 14. Distortion correction produced a small improvement in accuracy in all four cases. This improvement is significant for the clinical data but not the phantom data.[11]

We investigated temporal change in CT-physical registration accuracy using serially localized target marker positions obtained during two phantom experiments and surgical procedures performed on 24 patients in clinical trial Phase II. CT-physical TRE at time t was calculated using the target marker position localized at time t and the registration transformation determined at time zero. For the phantom experiments, the registration accuracy degraded gradually over time (see Fig. 15). The TRE at ten hours (mean ± SD = 0.88 ± 0.40 mm) is slightly and significantly higher than the TRE at time zero (0.58 ± 0.28 mm).[11] Repositioning of the OPS had negligible apparent effect on accuracy. The clinical results are pooled into eight groups of approximately 30 observations each (see Fig. 15). Registration accuracy deteriorated in the first hour after which there is no visually obvious trend. The TRE calculated by pooling all observations made after the first hour (1.50 ± 0.73 mm) is slightly and significantly higher than the TRE in the first 30 min (1.04 ± 0.46 mm).[10]

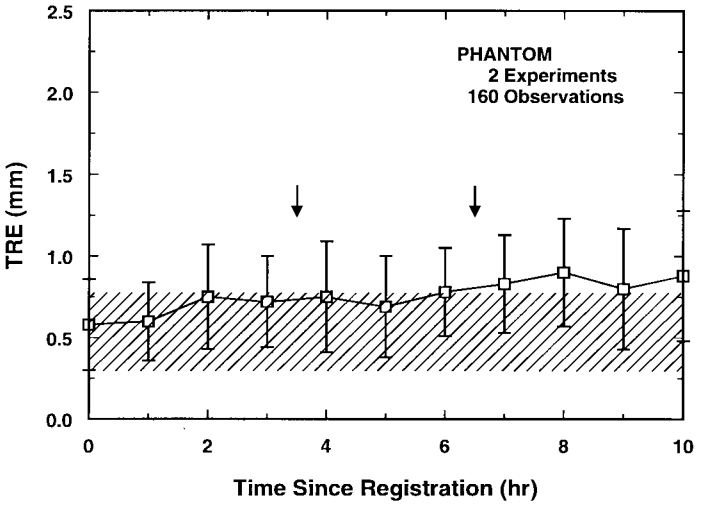

(a)

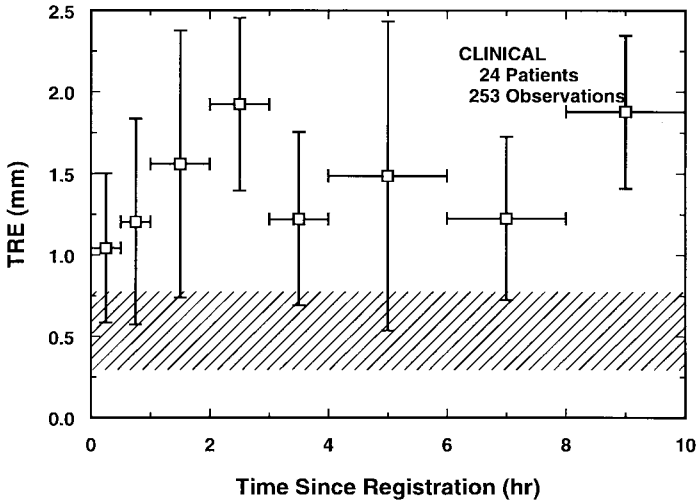

(b)

Fig. 15. Temporal change in CT-physical registration accuracy. (a) For the phantom experiments at two sites, physical space localization was repeated once per hour for ten hours. During these experiments, the OPS was moved one or two feet between hours 3 and 4 and again between hours 6 and 7 (indicated with arrows) to simulate the repositioning that is occasionally necessary intraoperatively, e.g., to maintain an optical line of sight. (b) For 24 patients in Phase II, physical space localization of the target marker was repeated several times during surgery. The results are pooled into eight groups of approximately 30 observations each. The horizontal bars indicate the time interval over which a group is pooled. For both the phantom and clinical data, all TRE values are calculated using the registration transformation determined at time zero. The symbols and vertical error bars represent mean ± SD. The hatched areas represent theoretical TRE_{OV} (phantom) or TRE_{OS} (clinical) values (mean ± SD) predicted by numerical simulation.

IV. Discussion

A. Design Issues and Comparison with Other Work

Stereotactic frame systems generally include a stereotactic reference frame that provides rigid skull fixation using pins or screws and establishes a stereotactic coordinate system in physical space, a method for stereotactic image acquisition, and a system for mechanical direction of a probe or other surgical instrument to a defined intracranial point [12], [20], [27]. Most current systems relate image space to the physical coordinate space established by the reference frame by attaching a localizing system consisting of N-shaped fiducials during image acquisition. Frames permit neurosurgeons to perform biopsies and to resect deep-seated and previously inaccessible lesions. Frame-based techniques, however, have several limitations. The frames are bulky and may interfere with the

[11] Two-tailed paired t-test, $p = 0.05$.

surgical exposure. Patients complain about the weight of the frame and the pain associated with its application. The surgeon is typically limited to target points on a linear trajectory. And, perhaps most importantly, frame-based stereotactic systems do not provide real-time feedback to the surgeon about anatomical structures encountered in the surgical field. To address these limitations, a number of frameless stereotactic systems have been developed over the last decade beginning with Roberts *et al.* in 1986 [10], [43].

Registration of preoperative images with the physical space occupied by the patient during surgery is a fundamental step in interactive, image-guided surgery techniques. Of the many frameless methods that have been used to register medical images (see [36], [53] for a review), point-based and surface-based methods are the most useful for IP registration. Point-based registration was described in Section II. Surface-based registration involves the determination of a corresponding surface in the image and physical space and the estimation of a geometrical transformation using these corresponding structures [8], [18], [46], [51]. A physical space surface map of the skin is created by sweeping the skin with a 3-D spatial digitizer [46], [51] or using an array of video cameras to detect patterned light [8], [18]. Then a search is performed to find the transformation that minimizes some cost function.

Point-based registration can be performed using either external landmarks such as the nasion and medial and lateral canthi or artificially applied markers such as glass beads or vitamin E capsules [10], [43]. Anatomical landmarks can be difficult to identify accurately. Because the skin is a movable and deformable structure, the position of markers that are affixed to it can change between imaging and registration in the operating room. Also, fixation by the Mayfield clamp distorts the scalp, especially in patients with loose skin. It is generally accepted that external landmarks and skin-based markers do not provide sufficient accuracy for some stereotactic procedures. For example, here are relevant excerpts from the conclusions of two recent papers.

> These results suggest that for procedures that require localization precision similar to that achievable with a stereotactic frame, a rigidly mounted marker system is to be preferred to the matching of anatomical landmarks [41].

> We have shown that the simple procedure of subcutaneous implant of short gold wires in the scalp does not provide a stable reference system in some patients and that screws embedded in the skull do [25].

To achieve a high level of accuracy, we thus, opted to use rigidly mounted markers. We initially considered metallic implants since they have a long history of use. For example, tantalum pins and spheres have been used to study bone movement and growth since 1955 [3], [45], [48]. More recently, titanium screws and pins were used to register CT images with physical space for stereotactic radiotherapy [25] and robot-assisted total hip replacement surgery [52]. Unfortunately metallic implants cause substantial geometrical and intensity distortion in MR images due to magnetic susceptibility differences between metal and tissue. Since we are interested in using MR (and also PET) images as well as CT, metallic implants are not suitable markers for our system. Hence we designed a marker consisting of various attachments that fit on a plastic base that is screwed into the skull. One attachment is an imageable marker that is bright in CT and MR. We have previously used an imageable marker filled with ^{18}F-fluorodeoxyglucose that is bright in PET. Another attachment is a localization cap (physical space marker) manufactured with a hemispherical divot whose position corresponds to the centroid of the image markers. The image fiducial (centroid of marker in image) thus, corresponds identically to the physical space fiducial (center of hemispherical divot). We believe that the liquid-filled image marker in conjunction with the localization cap provides the first multimodal implantable marker system, though an independently developed marker similar to this system has recently been reported [29].

The TRE of a point-based registration method is a function of the number of fiducials, their configuration, the FLE in each space, and the position of the target. The numerical simulations we performed show that for fiducials positioned on the surface of a sphere, mean TRE averaged over the volume inside the sphere is directly proportional to $\mathrm{FLE}_{\mathrm{eff}}$ and inversely proportional to the square root of the number of fiducials. Specifically

$$\text{mean TRE}_{\mathrm{TV}} = 1.64\,k\,\frac{\mathrm{FLE}_{\mathrm{eff}}}{\sqrt{N_f}} \tag{3}$$

where $k \geq 1$ is a function of the fiducial configuration, $\mathrm{FLE}_{\mathrm{eff}}$ is the effective FLE defined by (2), and N_f is the number of fiducials. Accurate point-based registration, thus, requires fiducials that can be localized accurately and/or many fiducials. Note that having many fiducials does not help when there is correlated motion (e.g., skin-based markers).

Our system is based on extrinsic markers attached to bases screwed into the skull. Because these markers are invasive, it is not desirable or feasible to use a large number of them. We must use at least three markers because a unique rigid-body transformation exists if and only if there are three noncollinear fiducials in the two spaces being registered. We chose to use four markers rather than three not only to reduce mean $\mathrm{TRE}_{\mathrm{TV}}$ but also to guarantee that there are a sufficient number of markers to compute a transformation if one of the markers becomes unusable.[12] In the clinical trial, a technical problem prevented the use of one marker in eight of the 158 operations, i.e., approximately 5% of the operations. Thus, using at least four markers provides a redundancy that is clinically important. Also, registrations computed using four markers are approximately 15% more accurate than registrations using three markers. Because we use a small number of markers, we had to focus on keeping both k and FLE small. Our system is accurate because we managed to do this successfully.

The fiducial configuration parameter k equals 1.0 for an optimal placement of fiducials on the surface of a sphere.

[12] We used a fifth marker in the clinical trial as a target for assessment of registration accuracy. Though a surgeon could potentially implant as many markers as he wishes, we currently believe that our system will generally be used with four markers.

For four markers optimal configurations are both a tetrahedral arrangement and a uniform distribution around the circumference. The value of k increases as the fiducials are distributed less evenly around the head (see Fig. 11).[13] Our simulations show that if the fiducials are placed in a "2-2" configuration, i.e., two fiducials are positioned on each side of the head, $k < 1.5$ if $d > 50$ mm, where d is the larger of the distances between fiducials on the two sides. If the fiducials are placed in a 3-1 configuration, $k < 1.5$ if $d > 75$ mm, where d is the maximum distance between any two of the three fiducials that are on one side of the head. Thus, we believe that accurate registrations-mean $\mathrm{TRE_{TV}} < 1.2\ \mathrm{FLE_{eff}}$ ($k < 1.5$) can be achieved in practice with four markers using the following relatively simple fiducial placement strategy.

> Place two markers at least 75 mm apart. Place the third marker on the opposite side of the head from the mid-point of the first two markers. Place the fourth marker anywhere, but preferably on the same side of the head as the third marker (though a 2-2 configuration is not appreciably more accurate than a 3-1 configuration, the latter can become a 3-0 configuration if one of the markers becomes unusable).

Markers should not be placed on only one side of the head unless surgery will be performed on that side. In this case, an approximately collinear arrangement should be strictly avoided.

$\mathrm{FLE_I}$ is the root-mean-square error in determining the position of an image marker. We have previously estimated the $\mathrm{FLE_I}$ of various marker designs by means of numerical simulation [57]. We found that it is possible to estimate the position of a marker with subvoxel precision if the marker is sufficiently (noise reduces the accuracy) larger than a voxel, and if partial volume information is exploited by using an intensity-weighted centroid. For example, the theoretical $\mathrm{FLE_I}$ of an infinitely small marker whose location within a voxel is randomly (uniformly) distributed is

$$\mathrm{FLE_I} = \sqrt{\frac{\Delta x_v^2 + \Delta y_v^2 + \Delta z_v^2}{12}} \tag{4}$$

where Δx_v, Δy_v, and Δz_v are the dimensions of an image voxel. For an image with voxel dimensions $0.5 \times 0.5 \times 4.0$ mm (typical of the images used in this study), the theoretical $\mathrm{FLE_I}$ of a small marker is approximately 1.2 mm. The imageable part of our marker is a cylinder with diameter 7 mm and height 5 mm. For the types of images used in this study, i.e., CT and MR images with slice thickness 3 to 5 mm, the $\mathrm{FLE_I}$ of our marker is approximately 0.4 mm [38], [39]. It is considerably better than the theoretical $\mathrm{FLE_I}$ of small markers, thus, confirming the theoretically predicted advantage of larger markers in producing smaller $\mathrm{FLE_I}$'s [4], [7], [57].

A critical component in any frameless stereotactic system is the method of physical space localization. Many such techniques have been developed. Many of the early frameless stereotactic systems used articulated mechanical arms [1], [13], [15], [28]. The position of the tip of an arm is calculated from the angles of its various joints. These systems are extremely accurate [9], [13], [15], but can be somewhat awkward to handle. Ultrasonic rangefinding systems use small spark gaps mounted on surgical instruments that emit ultrasonic signals [10], [43]. Time delays between emission of the signal and its detection by an array of three or more microphones are used to compute the position of each spark gap. Unfortunately, since the velocity of sound is a function of temperature and humidity, ultrasonic systems are sensitive to temperature and humidity variations. These systems may also be degraded by the presence of extraneous ultrasonic noise and echoes. Electromagnetic localization systems use sensors mounted on surgical instruments [26]. The position and orientation of an instrument is computed from the signal induced in the sensor by a low-frequency electromagnetic field source. Unfortunately the performance of these systems degrades around large metal objects. We chose an optical triangulation system that is extremely accurate—$\mathrm{FLE_P}$ is approximately 0.3 mm—and fairly easy to use. Optical systems require a clear line of sight between the OPS and surgical instrument. We found that the OPS occasionally needs to be repositioned but that generally the line of sight requirement is not a practical limitation. It should be possible to use redundant optical sensors (i.e., more than the three 1-D CCD arrays we currently use) mounted over the surgical field. We note that whereas we use an OPS to track IRED's mounted on the handle of a surgical probe, others use an array of video cameras to detect patterned light or a characteristic pattern on the handle [8], [18], [21], [51].

B. Clinical Accuracy and Sources of Error

There are several sources of error in a surgical navigation system: error inherent in the registration process, geometrical distortion in the images, movement of the patient during scanning, movement of the patient with respect to the system during surgery, and movement of the brain between scanning and surgery. An examination and comparison of the theoretical, experimental, and clinical results in this study reveals some information about the magnitude of the first four kinds of errors.

1) Error Inherent in the Registration Process: For an optimal distribution of four markers on the surface of the head, the mean theoretical "true" registration error predicted by numerical simulation is ∼0.3–0.4 mm.[14] When markers not used to estimate the transformation are used to calculate registration accuracy, the mean theoretical "observed" registration error is ∼0.5–0.6 mm.[14] This error is comparable to that which we observed for CT-physical registration in the phantom experiments, which means that the system functions as expected in the laboratory. The distribution of markers used as fiducials in the phantom experiments was close to optimal. The distribution of markers used as fiducials in the clinical trial was less than optimal but was generally within the guidelines of the fiducial placement strategy recommended above. For such clinically practical distributions, the mean theoretical "true" and "observed" registration errors are ∼0.5–0.6 and

[13]The value of k is also greater than one if the fiducials are distributed inside the volume of the sphere rather than on the surface as is the case with point-based registration using internal anatomical landmarks [22].

[14]This is approximately true for both volume-averaged and surface-averaged TRE and for both II and IP registration.

$\sim$0.7–0.8 mm, respectively.[14] The latter is comparable to the error we observed for CT-physical registration in Phase I, which means that the system also functions as expected in the operating room. An observed error that is higher than this suggests that there may be some additional source of error.

2) Geometrical Distortion in the Images: The effect of geometrical distortion in MR on registration accuracy is demonstrated in Table IV and Fig. 14. The error observed for CT-MR and MR-physical registration in the phantom experiments and Phase I using MR images that are corrected for distortion is comparable to the theoretically predicted error. Thus, the effect of geometrical distortion in MR in this study is $\sim$0.2–0.3 mm. We note, however, that this measurement takes no account of object-induced geometrical distortion (i.e., distortion due to magnetic susceptibility difference) near air-tissue interfaces inside the head. Such distortion can be calculated to be as high as $\sim$1–2 mm for typical readout gradient strengths. We have previously observed $\sim$3-mm misregistration of an anatomical landmark due to MR distortion (see Fig. 6 in [35]). Finally, we note that simple scale distortion of $\sim$1%, which is well within the manufacturer specifications of most MR machines, can cause $\sim$1-mm misregistration at the surface of the head. Though we took no special precautions in this study, we believe that quality assurance phantom testing should become a standard feature of any stereotactic system.

3) Movement of the Patient During Scanning: Patients in Phase I had a stereotactic frame applied. The frame was attached to the scanner table during image acquisition and, thus, served as a head fixation device. Patients in Phase II did not have a frame applied. Thus, differences in accuracy observed in the two phases of the clinical trial help quantify the effect of head movement during scanning without rigid head fixation. The error of MR-physical registration in Phase I and Phase II is virtually identical, indicating that head movement during MR scanning is not much of a problem. This is expected because of the nature of MR image formation. Patient movement during scanning will appear as blurring and other motion artifact, thus, degrading image quality, but will not in general affect geometrical fidelity or $\mathrm{FLE_I}$ unless the artifact is so serious as to make the image unusable. The error of CT-MR and CT-physical registration in Phase II is $\sim$0.3–0.5-mm higher than in Phase I. Because CT image volumes are stacks of sequentially acquired slices, any patient movement between slices distorts the image. Most of the CT scans acquired in the clinical trial are conventional scans. In addition to the normal difficulties of keeping a person still, head movement can be caused by inertial jerking during table advance. Helical (spiral) CT involves continuous patient translation during X-ray source rotation and produces a complete image volume in a relatively short period of time [19]. Thus, helical CT might significantly reduce head movement during scanning. There is also some preliminary work indicating that it might be possible to correct for patient movement during a helical CT scan [55], [56]. We note that helical CT has already replaced conventional CT in some clinical applications that require high image resolution and minimal patient movement [50], [54]. In summary, the effect of patient movement without rigid head fixation during MR scanning is negligible and during CT scanning is $\sim$0.3–0.5 mm. It might be possible to improve the latter with helical CT.

4) Movement of the Patient with Respect to the System During Surgery: The temporal change in registration accuracy during surgery is illustrated in Fig. 15. For the phantom experiments, the registration accuracy degraded gradually over time. The TRE at 10 h is $\sim$0.3-mm higher than the TRE at time zero. As expected, repositioning of the OPS had a negligible apparent effect on accuracy. For the clinical trial data, registration accuracy deteriorated in the first hour after which there is no visually obvious trend. The TRE calculated by pooling all observations made after the first hour is $\sim$0.5-mm higher than the TRE in the first 30 min. This comparison is naturally suggested by inspection of the data and the fact that the craniotomy was usually elevated $\sim$30–60 min after registration. The degradation in accuracy is probably due to patient movement within the Mayfield clamp, some of which may occur during elevation of the craniotomy. The degradation is variable, as shown by the large standard deviations in Fig. 15. Thus, whereas the mean change in TRE was $\sim$0.5 mm, a change $>$1 mm was observed in nine of 24 (38%) patients, and a change $>$1.5 mm was observed in three of 24 (13%). A somewhat comparable degradation in accuracy during surgery has been reported by [17]. Reregistration during surgery is somewhat difficult with our system since the markers are generally not in the sterile field. One possible solution is to make three or more bone divots before elevating the craniotomy. These divots can be used both for periodic monitoring of registration accuracy during surgery and for reregistration if necessary. Alternatively, a reference emitter can be rigidly affixed to the head [46].

5) Movement of the Brain Between Scanning and Surgery: The brain can move relative to the skull and, thus, relative to the markers since they are implanted in the bone. Movement of the brain between scanning and surgery or during surgery adds a source of error to the localization of anatomical structures in the surgical field that is not reflected by the TRE we have measured. The amount of brain movement is controversial. The brain is known to pulsate, and parenchymal excursions up to 0.5 mm in temporal synchrony with systole have been observed [42]. But pulsatile motion is of little concern since it is periodic and small. Some brain deformation clearly occurs after removal of volume (e.g., cyst drainage, tumor resection) [17], [46]. Brain movement may also occur as a result of brain volume changes caused by presurgical administration of steroids to reduce inflammation and intraoperative interventions such as manipulation of inhaled CO_2 concentration and administration of osmotically active agents (e.g., mannitol). Brain movement is unlikely to be a problem for stereotactic radiosurgery, procedures that involve small burr holes (e.g., stereotactic biopsy), and procedures that involve nondeformable anatomy (e.g., skull base surgery). The effect of brain movement on the accuracy of surgical navigation in other cases is unclear. If brain movement turns out to be important, it may be possible to correct for it using video or ultrasound. These issues are an active area of research (e.g., [5], [23]).

ACKNOWLEDGMENT

The authors wish to thank the following individuals for their kind and generous assistance (departments when listed are at Vanderbilt University, Nashville, TN): M. S. Berger (University of Washington, Seattle, WA); H. Chang (General Electric Corporate Research & Development, Schenectady, NY); F. A. Collins (Collins Associates Incorporated, Medfield, MA); B. Copeland (Scripps Clinic, La Jolla, CA); D. G. Crouch (Northern Digital, Inc., Waterloo, Ont., Canada); S. Dong (University of Pennsylvania, Philadelphia, PA); S. Gadamsetty (Department of Electrical Engineering); D. Goins (Department of Radiology); A. Jackson (Department of Radiology); J. W. Kingsley (Department of News and Public Affairs); V. R. Mandava (C. S. First Boston, Tokyo, Japan); J. J. McCrory (Boston Scientific, Natick, MA); P. Monteiro (Johnson & Johnson Professional, Inc., Raynham, MA); C. B. Paschal (Department of Biomedical Engineering); R. R. Price (Department of Radiology); R. S. Randall (Johnson & Johnson Professional, Inc.); D. N. Rowitch (Science Applications International Corp., San Diego, CA); R. G. Selker (Western Pennsylvania Hospital, Pittsburgh, PA); C. Southworth (Johnson & Johnson Professional, Inc.); M. R. Willcott (University of Texas Medical Branch at Galveston, Galveston, TX). C. R. Maurer was with the Department of Biomedical Engineering while much of this work was performed

REFERENCES

[1] L. Adams, W. Krybus, D. Meyer-Ebrecht, R. Rueger, J. M. Gilsbach, R. Moesges, and G. Schloendorff, "Computer-assisted surgery," *IEEE Comput. Graph. Appl.*, vol. 10, pp. 43–51, 1990.

[2] K. S. Arun, T. S. Huang, and S. D. Blostein, "Least-squares fitting of two 3-D point sets," *IEEE Trans. Pattern Anal. Machine Intell.*, vol. PAMI-9, pp. 698–700, 1987.

[3] A. Björk, "Facial growth in man, studied with the aid of metallic implants," *Acta Odontol. Scand.*, vol. 13, pp. 9–34, 1955.

[4] C. B. Bose and I. Amir, "Design of fiducials for accurate registration using machine vision," *IEEE Trans. Pattern Anal. Machine Intell.*, vol. PAMI-12, pp. 1196–1200, 1990.

[5] R. D. Bucholz, D. D. Yeh, J. Trobaugh, L. L. McDurmont, C. D. Sturm, C. Baumann, J. M. Henderson, A. Levy, and P. Kessman, "The correction of stereotactic inaccuracy caused by brain shift using an intraoperative ultrasound device," in *CVRMed-MRCAS '97*, J. Troccaz, E. Grimson, and R. Mösges, Eds. Berlin, Germany: Springer-Verlag, 1997, pp. 459–466.

[6] H. Chang and J. M. Fitzpatrick, "A technique for accurate magnetic resonance imaging in the presence of field inhomogeneities," *IEEE Trans. Med. Imag.*, vol. 11, pp. 319–329, 1992.

[7] G. Chiorboli and G. P. Vecchi, "Comments on 'Design of fiducials for accurate registration using machine vision'," *IEEE Trans. Pattern Anal. Machine Intell.*, vol. 15, pp. 1330–1332, 1993.

[8] A. C. F. Colchester, J. Zhao, K. S. Holton-Tainter, C. J. Henri, N. Maitland, P. T. E. Roberts, C. G. Harris, and R. J. Evans, "Development and preliminary evaluation of VISLAN, a surgical planning and guidance system using intra-operative video imaging," *Med. Image Anal.*, vol. 1, pp. 73–90, 1996.

[9] C. A. Edwards, II and R. L. Galloway, Jr., "A single-point calibration technique for a six degree-of-freedom articulated arm," *Int. J. Robot. Res.*, vol. 13, pp. 189–198, 1994.

[10] E. M. Friets, J. W. Strohbehn, J. F. Hatch, and D. W. Roberts, "A frameless stereotaxic operating microscope for neurosurgery," *IEEE Trans. Biomed. Eng.*, vol. 36, pp. 608–617, 1989.

[11] R. L. Galloway, Jr., C. A. Edwards, II, J. T. Lewis, and R. J. Maciunas, "Image display and surgical visualization in interactive image-guided neurosurgery," *Opt. Eng.*, vol. 32, pp. 1955–1962, 1993.

[12] R. L. Galloway, Jr., and R. J. Maciunas, "Stereotactic neurosurgery," *Crit. Rev. Biomed. Eng.*, vol. 18, pp. 207–233, 1990.

[13] ——, "An articulated localizing arm for neurosurgical use," in *Interactive Image-Guided Neurosurgery*, R. J. Maciunas, Ed. Park Ridge, IL: Amer. Assoc. Neurological Surgeons, 1993, pp. 159–168..

[14] R. L. Galloway, Jr., R. J. Maciunas, W. A. Bass, and D. Crouch, "An optical device for interactive, image-guided neurosurgery," in *Proc. Annu. Int. Conf. IEEE Eng. Med. Biol. Soc.*, 1993, vol. 15, pp. 954–955.

[15] R. L. Galloway, Jr., R. J. Maciunas, and C. A. Edwards, II, "Interactive image-guided neurosurgery," *IEEE Trans. Biomed. Eng.*, vol. 39, pp. 1226–1231, 1992.

[16] S. K. Ghosh, *Analytical Photogrammetry*, 2nd ed. New York: Pergamon, 1988.

[17] J. G. Golfinos, B. C. Fitzpatrick, L. R. Smith, and R. F. Spetzler, "Clinical use of a frameless stereotactic arm: Results of 325 cases," *J. Neurosurg.*, vol. 83, pp. 197–205, 1995.

[18] W. E. L. Grimson, G. J. Ettinger, S. J. White, T. Lozano-Perez, W. M. Wells, III, and R. Kikinis, "An automatic registration method for frameless stereotaxy, image guided surgery, and enhanced reality visualization," *IEEE Trans. Med. Imag.*, vol. 15, pp. 129–140, 1996.

[19] J. P. Heiken, J. A. Brink, and M. W. Vannier, "Spiral (helical) CT," *Radiol.*, vol. 189, pp. 647–656, 1993.

[20] M. P. Heilbrun, Ed., *Stereotactic Neurosurgery*. Baltiore, MD: , Williams & Wilkins, 1988.

[21] M. P. Heilbrun, S. Koehler, P. McDonald, W. Peters, V. Sieminov, and C. Wiker, "Implementation of a machine vision method for stereotactic localization and guidance," in *Interactive Image-Guided Neurosurgery*, R. J. Maciunas, Ed. Park Ridge, IL: Amer. Assoc. Neurological Surgeons, 1993, pp. 169–177.

[22] D. L. G. Hill, D. J. Hawkes, M. J. Gleeson, T. C. S. Cox, A. J. Strong, W.-L. Wong, C. F. Ruff, N. Kitchen, D. G. T. Thomas, J. E. Crossman, C. Studholme, A. J. Gandhe, S. E. M. Green, and G. P. Robinson, "Accurate framless registration of MR and CT images of the head: Applications in surgery and radiotherapy planning," *Radiol.*, vol. 191, pp. 447–454, 1994.

[23] D. L. G. Hill, C. R. Maurer, Jr., M. Y. Wang, R. J. Maciunas, J. Barwise, and J. M. Fitzpatrick, "Estimation of intraoperative brain surface movement," in *CVRMed-MRCAS '97*, J. Troccaz, E. Grimson, and R. Mösges, Eds. Berlin, Germany: Springer-Verlag, 1997, pp. 449–458.

[24] J. R. Hurley and R. B. Cattell, "The Procrustes program: Producing direct rotation to test a hypothesized factor structure," *Behav. Sci.*, vol. 7, pp. 258–262, 1962.

[25] D. Jones, D. A. Christopherson, J. T. Washington, M. D. Hafermann, J. W. Rieke, J. J. Travaglini, and S. S. Vermeulen, "A frameless method for stereotactic radiotherapy," *Br. J. Radiol.*, vol. 66, pp. 1142–1150, 1993.

[26] A. Kato, T. Yoshimine, T. Hayakawa, Y. Tomita, T. Ikeda, M. Mitomo, K. Harada, and H. Mogami, "A frameless, armless navigational system for computer-assisted tomography," *J. Neurosurg.*, vol. 74, pp. 845–849, 1991.

[27] P. J. Kelly, *Tumor Stereotaxis*. Philadelphia, PA: Saunders, 1991.

[28] Y. Kosugi, E. Watanabe, J. Goto, T. Watanabe, S. Yoshimoto, K. Takakura, and J. Ikebe, "An articulated neurosurgical navigation system using MRI and CT images," *IEEE Trans. Biomed. Eng.*, vol. 35, pp. 147–152, 1988.

[29] C. Kremser, C. Plangger, R. Bösecke, A. Pallua, F. Aichner, and S. Felber, "New marker system for frameless image registration," in *Proc. Soc. Magn. Reson.*, 1995, p. 1163.

[30] S. Lavallee, P. Sautot, J. Troccaz, P. Cinquin, and P. Merloz, "Computer-assisted spine surgery: A technique for accurate transpedicular screw fixation using CT data and a 3-D optical localizer," *J. Image Guid. Surg.*, vol. 1, pp. 65–73, 1995.

[31] J. T. Lewis and R. L. Galloway, Jr., "Ultrasonic detection of subcutaneous fiducial markers for image-physical space registration," in *Proc. Annu. Int. Conf. IEEE Eng. Med. Biol. Soc.*, 1992, vol. 14, pp. 1061–1062.

[32] R. J. Maciunas, M. S. Berger, B. Copeland, M. R. Mayberg, R. G. Selker, J. M. Fitzpatrick, R. L. Galloway, Jr., C. R. Maurer, Jr., and G. S. Allen, "A prospective, blinded, multicenter trial of objective medical image registration," *J. Neurosurg.*, submitted for review.

[33] V. R. Mandava, J. M. Fitzpatrick, C. R. Maurer, Jr., R. J. Maciunas, and G. S. Allen, "Registration of multimodal volume head images via attached markers," in *Proc. SPIE Medical Imaging VI: Image Processing*, 1992, vol. 1652, pp. 271–282.

[34] V. R. Mandava, R. J. Maciunas, J. M. Fitzpatrick, R. L. Galloway, Jr., and C. R. Maurer, Jr., "A workstation platform for stereotactic neurosurgical planning," *Proc. Annu. Int. Conf. IEEE Eng. Med. Biol. Soc.*, vol. 13, pp. 1220–1221, 1991.

[35] C. R. Maurer, Jr., G. B. Aboutanos, B. M. Dawant, S. Gadamsetty, R. A. Margolin, R. J. Maciunas, and J. M. Fitzpatrick, "Effect of geometrical

distortion correction in MR on image registration accuracy," *J. Comput. Assist. Tomogr.*, vol. 20, pp. 666–679, 1996.
[36] C. R. Maurer, Jr. and J. M. Fitzpatrick, "A review of medical image registration," in *Interactive Image-Guided Neurosurgery*, R. J. Maciunas, Ed. Park Ridge, IL: Amer. Assoc. Neurological Surgeons, 1993.
[37] C. R. Maurer, Jr., J. M. Fitzpatrick, R. L. Galloway, Jr., M. Y. Wang, R. J. Maciunas, and G. S. Allen, "The accuracy of image-guided neurosurgery using implantable fiducial markers," in *Computer Assisted Radiology 1995*, H. U. Lemke, K. Inamura, C. C. Jaffe, and M. W. Vannier, Eds. Berlin, Germany: Springer-Verlag, 1995, pp. 1197–1202.
[38] C. R. Maurer, Jr., J. M. Fitzpatrick, M. Y. Wang, and R. J. Maciunas, "Estimation of localization accuracy for markers in multimodal volume images," in *Proc. Annu. Int. Conf. IEEE Eng. Med. Biol. Soc.*, 1993, vol. 15, pp. 124–125.
[39] C. R. Maurer, Jr., J. J. McCrory, and J. M. Fitzpatrick, "Estimation of accuracy in localizing externally attached markers in multimodal volume head images," in *Proc. SPIE Medical Imaging 1993: Image Processing*, 1993, vol. 1898, pp. 43–54.
[40] *Accuracy of Digitizing Probes*, Northern Digital, Inc., Waterloo, Ont., Canada, May 1992.
[41] T. Peters, B. Davey, P. Munger, R. Comeau, A. Evans, and A. Olivier, "Three-dimensional multimodal image-guidance for neurosurgery," *IEEE Trans. Med. Imag.*, vol. 15, pp. 121–128, 1996.
[42] B. P. Poncelet, V. J. Wedeen, R. M. Weisskoff, and M. S. Cohen, "Brain parenchyma motion: Measurement with cine echoplanar MR imaging," *Radiol.*, vol. 185, pp. 645–651, 1992.
[43] D. W. Roberts, J. W. Strohbehn, J. F. Hatch, W. Murray, and H. Kettenberger, "A frameless stereotaxic integration of computerized tomographic imaging and the operating microscope," *J. Neurosurg.*, vol. 65, pp. 545–549, 1986.
[44] R. Rohling, P. Munger, J. M. Hollerbach, and T. Peters, "Comparison of relative accuracy between a mechanical and an optical position tracker for image-guided neurosurgery," *J. Image Guid. Surg.*, vol. 1, pp. 30–34, 1995.
[45] B. Rune, K.-V. Sarnäs, G. Selvik, and S. Jacobsson, "Roentgen stereometry with the aid of metallic implants in hemifacial microsomia," *Amer. J. Orthod.*, vol. 84, pp. 231–247, 1983.
[46] M. J. Ryan, R. K. Erickson, D. N. Levin, C. A. Pelizzari, R. L. MacDonald, and G. J. Dohrmann, "Frameless stereotaxy with real-time tracking of patient head movement and retrospective patient-image registration," in *Medical Robotics and Computer Assisted Surgery 1995*. New York: Wiley-Liss, 1995, pp. 1–7.
[47] P. H. Schönemann, "A generalized solution of the orthogonal Procrustes problem," *Psychometrika*, vol. 31, pp. 1–10, 1966.
[48] G. Selvik, "A roentgen stereophotogrammetric method for the study of the kinematics of the skeletal system," Ph.D. thesis, Univ. Lund, Lund, Sweden, 1974.
[49] D. A. Simon, R. V. O'Toole, M. Blackwell, F. Morgan, A. M. DiGioia, and T. Kanade, "Accuracy validation in image-guided orthopaedic surgery," in *Medical Robotics and Computer Assisted Surgery 1995*. New York: Wiley-Liss, 1995, pp. 185–192.
[50] M. W. Skinner, D. R. Ketten, M. W. Vannier, G. A. Gates, R. L. Yoffie, and W. A. Kalender, "Determination of the position of nucleus cochlear implant electrodes in the inner ear," *Amer. J. Otol.*, vol. 15, pp. 644–651, 1994.
[51] K. K. Tan, R. Grzeszczuk, D. N. Levin, C. A. Pelizzari, G. T. Chen, R. K. Erickson, D. Johnson, and G. J. Dohrmann, "A frameless stereotactic approach to neurosurgical planning based on retrospective patient-image registration," *J. Neurosurg.*, vol. 79, pp. 296–303, 1993.
[52] R. H. Taylor, B. D. Mittelstadt, H. A. Paul, W. Hanson, P. Kazanzides, J. F. Zuhars, B. Williamson, B. L. Musits, E. Glassman, and W. L. Bargar, "An image-directed robotic system for precise orthopaedic surgery," *IEEE Trans. Robot. Automat.*, vol. 10, pp. 261–275, 1994.
[53] P. A. van den Elsen, E.-J. D. Pol, and M. A. Viergever, "Medical image matching: A review with classification," *IEEE Eng. Med. Biol. Mag.*, vol. 12, pp. 26–39, 1993.
[54] M. W. Vannier and G. Wang, "Spiral CT refines temporal bone imaging," *Diagn. Imaging*, vol. 15, pp. 116–121, 1993.
[55] G. Wang and M. W. Vannier, "Stair-step artifacts in three-dimensional helical CT: An experimental study," *Radiol.*, vol. 191, pp. 79–83, 1994.
[56] ———, "Preliminary study on helical CT algorithms for patient motion estimation and compensation," *IEEE Trans. Med. Imag.*, vol. 14, pp. 205–211, 1995.
[57] M. Y. Wang, J. M. Fitzpatrick, and C. R. Maurer, Jr., "Design of fiducials for accurate registration of CT and MR volume images," in *Proc SPIE Medical Imaging 1995: Image Processing*, 1995, vol. 2434, pp. 96–108.
[58] M. Y. Wang, C. R. Maurer, Jr., J. M. Fitzpatrick, and R. J. Maciunas, "An automatic technique for finding and localizing externally attached markers in CT and MR volume images of the head," *IEEE Trans. Biomed. Eng.*, vol. BME-43, pp. 627–637, 1996.